Journal of
Composites Science

MDPI

Article

Behavior of Pultruded Glass-Fiber-Reinforced Polymer Beam-Columns Infilled with Engineered Cementitious Composites under Cyclic Loading

Yoganantham Chinnasamy [1], Philip Saratha Joanna [2,*], Karthikeyan Kothanda [3], Beulah Gnana Ananthi Gurupatham [4] and Krishanu Roy [5,*]

1 School of Planning, Architecture and Design Excellence, Hindustan Institute of Technology and Science, Padur, Chennai 603103, India
2 Department of Civil Engineering, Hindustan Institute of Technology and Science, Padur, Chennai 603103, India
3 School of Civil Engineering, Vellore Institute of Technology, Chennai 600127, India
4 Department of Civil Engineering, College of Engineering Guindy Campus, Anna University, Chennai 600025, India
5 School of Engineering, The University of Waikato, Hamilton 3216, New Zealand
* Correspondence: joanna@hindustanuniv.ac.in (P.S.J.); krishanu.roy@waikato.ac.nz (K.R.)

Abstract: Glass-fiber-reinforced polymer (GFRP) is an advanced material that has superior corrosion resistance, a high strength-to-weight ratio, low thermal conductivity, high stiffness, high fatigue strength, and the ability to resist chemical and microbiological compounds. Despite their many advantages compared with traditional materials, GFRP sections exhibit brittle behavior when subjected to severe loading conditions such as earthquakes, which could be overcome by infilling the GFRP sections with concrete. This paper presents the results of an experimental investigation carried out on the cyclic response of a GFRP beam-column infilled with high-volume fly ash engineered cementitious composites (HVFA-ECC) consisting of 60%, 70%, and 80% fly ash as a replacement for cement. Finite element analysis was also conducted using robot structural analysis software, and the results were compared with the experimental results. The mechanical properties of GFRP sections presented are the compressive strength of ECC, the direct tensile strength of ECC determined using a dog-bone-shaped ECC specimen, the hysteresis behavior of the beam-column, and the energy dissipation characteristics. The lateral load-carrying capacity of beam-column GFRP infilled with HVFA-ECC consisting of 60%, 70%, and 80% fly ash was found to be, respectively, 43%, 31%, and 20% higher than the capacity of GFRP beam-columns without any infill. Hence the GFRP sections infilled with HVFA-ECC could be used as lightweight structural components in buildings to be constructed in earthquake-prone areas. Also in the structural components, as 70% of cement could be replaced with fly ash, it can potentially lead to sustainable construction.

Keywords: pultruded glass-fiber-reinforced polymer; engineered cementitious composite; high-volume fly ash; finite element analysis; cyclic loading

Citation: Chinnasamy, Y.; Joanna, P.S.; Kothanda, K.; Gurupatham, B.G.A.; Roy, K. Behavior of Pultruded Glass-Fiber-Reinforced Polymer Beam-Columns Infilled with Engineered Cementitious Composites under Cyclic Loading. *J. Compos. Sci.* **2022**, *6*, 338. https://doi.org/10.3390/jcs6110338

Academic Editor: Francesco Tornabene

Received: 23 September 2022
Accepted: 1 November 2022
Published: 4 November 2022

1. Introduction

Composites have started replacing traditional materials in most engineering fields, such as the aerospace, marine, automobile, electrical, chemical, and construction industries where high strength and stiffness-to-weight ratios are required. Fiber-reinforced polymer (FRP) is one of the composite materials in which fibers such as glass, aramid, and carbon are embedded in the matrix material. As FRP composites have high stiffness, light weight, corrosion resistance, and chemical resistance, they are being utilized in the construction industry. In FRP sections, fibers carry the load and the matrix protects the fibers from the atmosphere and also helps in transferring load to the fibers. Carbon and graphite fibers are

light in weight and stronger than other fibers. However, the cost of carbon fibers is higher than that of glass or aramid fibers. Glass fibers are more ductile and cheaper than carbon fibers, which leads to their utility in the construction industry [1].

Pultruded glass-fiber-reinforced polymers (GFRP) are made with 12–35 m diameter glass fibers and are embedded with vinyl ester/polyester/epoxy resins through a continuous rowing method called the pultrusion process. The process consists of pulling impregnated filaments together with a mat or fabric through a heated die. The fiber composition and stiffness of GFRP sections vary with the manufacturer, and hence, it is very important to find the mechanical properties of GFRP sections with suitable test methods [2,3]. The load-carrying capacity and stiffness of the GFRP sections increase when infilled with concrete. Concrete-infilled GFRP tubes have a higher flexural strength than conventional reinforced concrete [4–7]. The GFRP tube confines the entire cross-section of the concrete, and longitudinal fibers act as reinforcement in the longitudinal direction of the beam [8]. Concrete-infilled glass-/carbon-fiber-reinforced polymer tubes could fail sequentially and progressively and exhibit pseudo-ductile behavior [9–14]. The use of high-grade concrete as an infill in GFRP sections exhibits only a 20% increase in load-carrying capacity compared to low-strength concrete as an infill [15–17].

Engineered cementitious composite (ECC) is a special type of concrete that exhibits increased tensile strength and strain-hardening behavior compared to conventional concrete. In ECC, strain-hardening takes place after the first cracking like a ductile metal and exhibits 3% to 5% tensile strain capacity, which is 300 to 500 times higher than that of normal concrete. ECC typically has a tensile strain capacity of more than 3% of compressive strength due to the interaction between fibers and matrix and exhibits closely spaced cracks, resulting in decreased water permeability or chloride ion penetration into the mixture [18]. ECC consists of cement, fine aggregates of a maximum size of 200 m, water, and high-range water-reducing (HRWR) admixture to increase workability and less than 2% volume of fibers. Different varieties of ECC with fibers such as polyvinyl alcohol (PVA), polypropylene (PP), and polyethylene (PE) fibers have been developed, and their properties have been investigated. ECC with PVA fibers exhibits higher tensile strength, toughness, and flexural strength than that of PP fibers. Further, the cost of PVA fiber is eight times less than that of PE fiber [19]. The elimination of coarse aggregate (CA) from ECC results in relatively higher cement content in the mixture and also leads to higher costs and environmental pollution. The production of one ton of cement emits 0.94 tons of CO_2 into the atmosphere, along with other glasshouse gases such as nitrogen oxide and sulfur dioxide. However, industrial solid waste materials such as fly ash (FA), ground granulated blast furnace slag (GGBS), silica fume (SF), and inert limestone powder could be added to ECC, which acts as a filler material and results in good workability, lower cement content, and a reduction in embodied carbon in ECC. The shear strength and ductility of concrete with cement replaced with FA are higher than those of cement replaced with GGBS and SF [20–24]. The use of FA in ECC results in substantial energy savings and decreases greenhouse gas emissions [25]. Further, the use of fly ash reduces the requirement for a large land area for its disposal, thus creating significant benefits for the environment. A feasible design approach was carried out in the development of ECC with FA of various quantities based on simple flow testing as a guideline [26–31]. There is a decrease in the strength of the ECC following an increase in fly ash content. Cracks with smaller widths were noticed when the fly ash content increased [32–34]. The use of fly ash in ECC contributes to the self-compactability of the fresh ECC and also helps in achieving the strain-hardening behavior of hardened ECC, which in turn leads to sustainability [35–38].

The durability of the concrete is greatly influenced by curing since it has a significant effect on the hydration process. Negligence in curing will hurt the strength and durability of concrete [39]. On the 7th and 28th days, the compressive and split tensile strength of concrete with 0.5, 1, and 1.5 percent polyethylene glycol (PEG-600) as an internal curing agent were tested and compared to conventional concrete [40]. PEG-600 in concrete not only helps with self-curing but also helps with better cement hydration and increases

compressive strength by trapping the moisture within the concrete, preventing it from evaporating [41]. An increase in the amount of PEG-600% in concrete decreases the strength of the concrete. As a result, adding 0.5% to 1% PEG-600 as an internal curing agent to concrete improves its effectiveness [42–44]. The literature available on ECC with HVFA is rather limited, and no literature is available on the effect of an internal curing agent on ECC with manufactured sand (M-sand).

In the construction industry, FRP composites have been used because of their high stiffness, lightweight, corrosion resistance, and easy installation. However, its utilization has a limitation because of its brittle failure. Hence, in this invention, the GFRP beam-column was infilled with the eco-friendly high-volume fly ash engineered cementitious composite. The present study is to investigate the mechanical properties of pultruded GFRP sections and to develop the ECC with HVFA, M-sand, and self-curing agent which is to be used as an infill in pultruded GFRP square sections, as well as to investigate the hysteretic behavior of beam-columns made of pultruded GFRP sections infilled with HVFA-ECC. Numerical investigations were carried out using Autodesk robot structural analysis (RSA) professional software to compare with the experimental investigation.

2. Materials and Methods

2.1. GFRP Sections

In this research, pultruded GFRP sections of size 100 mm × 100 mm, 5 mm thick, were used. The mechanical properties of the GFRP sections were carried out on coupons extruded from GFRP sections. Tensile, compressive, flexural, and shear strength tests were carried out on coupons extruded from GFRP sections as per ASTM D3039 [45], ASTM D3410 [46], ASTM D790 [47], and ASTM D2344 [48], respectively, as shown in Figure 1.

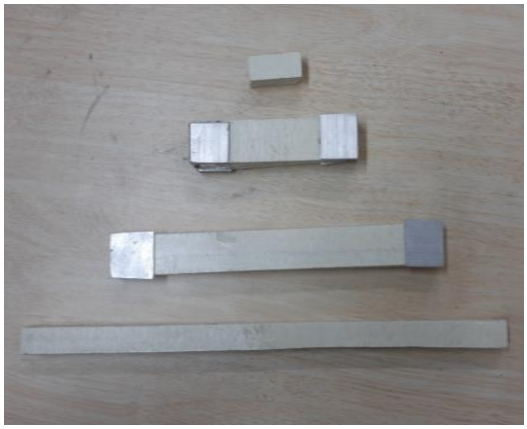

Figure 1. GFRP coupons.

All tests were carried out on a servo-controlled universal testing machine (UTM) of 100 kN capacity. Three specimens were prepared to conduct the test, and the details of the coupons extruded to find the mechanical properties of GFRP sections are given in Table 1.

Table 1. Details of the GFRP coupons.

Name of the Test	Coupon Size (mm)
Tensile strength	250 × 25 × 5
Compressive strength	125 × 25 × 5
Flexural strength	360 × 15 × 5
Interlaminar shear strength	50 × 15 × 5

The average ultimate tensile strength, compressive strength, elastic modulus, flexural strength, flexural modulus, shear strength, and shear modulus are 387.5 MPa, 150 MPa, 17.2 Mpa, 215 MPa, 1.1 GPa, 29 MPa, and 3 GPa, respectively.

2.2. Engineered Cementitious Composite with High-Volume Fly Ash (ECC-HVFA)

ECC contains ordinary Portland cement (OPC)-53 grade, manufactured sand (M-sand) having a size of 150–300 m, "Class F" fly ash, PVA fiber of 12 mm length, CONXL PCE RHEOPLUS 2635, a high-range water-reducing (HRWR) agent, and PEG 600, an internal curing agent. The properties of PVA fibers and PEG600 are given in Tables 2 and 3. In ECC, cement was replaced with fly ash ranging from 60% to 80%.

Table 2. Properties of PVA fibers.

Fibre	Density	Initial Modulus	Specification	Oil Agent Content
PVA	1.29	280 cN/dtex	12 mm	0.2%

Table 3. Properties of PEG-600 agent.

Sl. No	PEG600	
1	Solubility	Soluble in water
2	Density	1.126 kg/m^3
3	Odor	Mild odor
4	Mean molecular weight	570–630 kg/m^3
5	Appearance	Clear liquid

In a pan mixer, cement, fly ash, and M-sand were mixed for 5 to 6 min, and then HRWR and PEG 600 mixed with water were added gradually. The mixing continued for 10 to 15 min. After ensuring the minimum spread value using a mini-slump flow test, fibers were added to the mix, and the pan mixer was continuously rotated to avoid the formation of lumps in the mix. All the mixes were designed to have spread values of between 450 mm and 500 mm as stipulated in the standard slump flow test. A mini-slump cone test was carried out before the addition of fibers in ECC using a 60 mm high mini-slump cone. All the mixes were designed to ensure the achievement of a spread value of between 270 mm and 300 mm. A workability test for the final mix with fiber was carried out on a standard slump cone of 300 mm in height to find the flowability of ECC. All the mixtures were designed to ensure the achievement of spread values ranging from 450 mm to 500 mm. The workability test is shown in Figure 2. The mix proportion details of ECC are shown in Table 4.

(**a**) (**b**)

Figure 2. Workability test on ECC. (**a**) Mini-slump test; (**b**) standard slump test.

Table 4. Strength of concrete mixes.

Mix	Description	Cement to Binder (B)	Fly Ash to B	M-Sand to B	Water to B	HRWR to B	Fiber to B	PEG to B
1	ECC-0	1	0	0.6	0.35	0.005	0.01	0
2	ECC-60P	0.4	0.6	0.6	0.37	0.005	0.01	0.02
3	ECC-70P	0.3	0.7	0.6	0.4	0.005	0.01	0.02
4	ECC-80P	0.2	0.8	0.6	0.44	0.005	0.01	0.02

2.2.1. Mechanical Properties of HVFA-ECC

Compressive Strength

The compressive strength test on four mixes of ECC was carried out in the compression testing machine. The three cubes in each mix were tested at the ends of 7 days, 28 days, and 56 days after casting, and the average values were taken as the compressive strength of the mixes, as shown in Table 5.

Table 5. Compressive strength for different concrete mixes.

Mix	Mix Description	7 Days (MPa)	28 Days (MPa)	56 Days (MPa)
1	ECC-0	15.6	33.5	36.2
2	ECC-60P	12.9	28.7	34.5
3	ECC-70P	9.36	26.9	31.2
4	ECC-80P	6.01	23.7	28.4

The compressive strength of self-cured ECC-60P, ECC-70P, and ECC-80P was 20%, 66%, and 15% less than ECC-0 at 7 days. The compressive strength of self-cured ECC-60P, ECC-70P, and ECC-80P was, respectively, 16%, 25%, and 41% less than that of ECC-0 at 28 days, and 4%, 16%, and 27% less than that of ECC-0 at 56 days.

Direct Tensile Strength

The direct tensile strength of ECC was determined using a dog-bone-shaped specimen having an 80 mm gauge length with a 36 mm × 20 mm cross-section. Three dog-bone-shaped specimens were cast from the same batch of ECC. The specimens made of ECC-0 were cured with water, and the specimens of ECC-60P, ECC-70P, and ECC-80P added with self-curing agents were cured under shade. The detailed and direct tensile strength tests were carried out on a dog-bone-shaped specimen as shown in Figure 3 in UTM of 100 kN capacity as per ASTM C1273 [49].

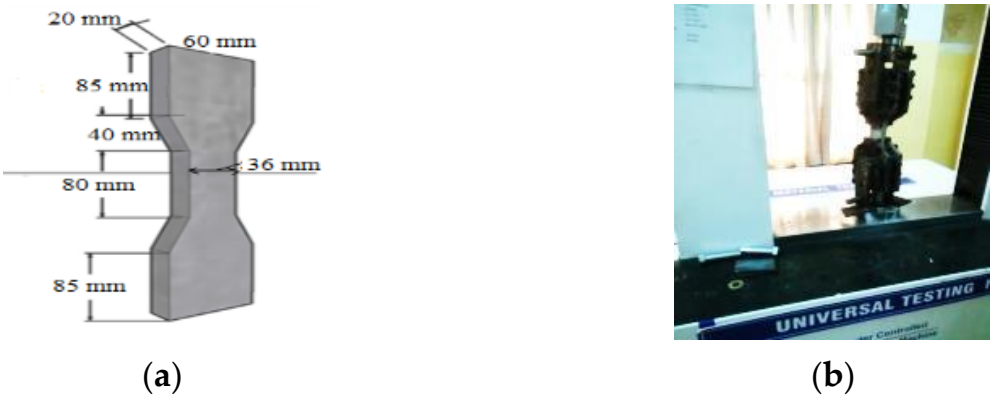

Figure 3. Direct tensile strength test setup. (**a**) Dog-bone-shaped specimen; (**b**) direct tensile strength test setup on ECC.

The rate of displacement of the crosshead was kept at 0.1 mm/min. The tensile strengths of three dog-bone-shaped specimens in each series of mixes were tested after

28 days of casting, and the average values were taken as the tensile strengths of ECC mixes. The tensile strength test results of all the mixes are shown in Table 6.

Table 6. Direct tensile test results.

Mix Description	Mix	Tensile Stress (MPa)		Tensile Strain (%)
		At Initial Crack	At Ultimate Level	Ultimate Level
ECC-0	2	4.40	4.80	1.22
ECC-60P	4	4.10	4.30	0.97
ECC-70P	7	4.05	4.15	0.97
ECC-80P	10	3.90	3.98	0.97

ECC with and without fly ash exhibited a fluctuation in the stress–strain curve due to the propagation of cracks during the time of loading. The ultimate tensile strength of ECC-60P, ECC-70P, and ECC-80P was, respectively, 7%, 9%, and 11.5% less than that of ECC-0, and the ultimate tensile strains of ECC-60P, ECC-70P, and ECC-80P were 20% less than that of ECC-0. The stress–strain curve obtained from a direct tensile strength test is shown in Figure 4.

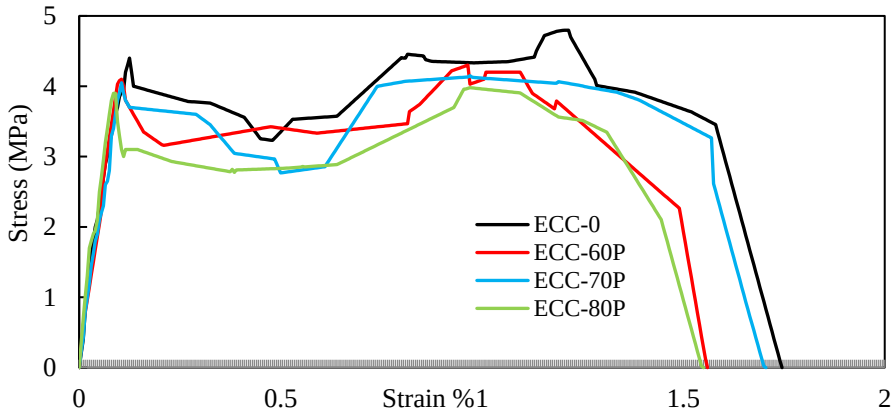

Figure 4. Stress–strain curves obtained from the direct tensile strength tests.

2.3. Beam-Column Specimens

Eight GFRP beam-column specimens having a beam of 1.5 m length and a column of 1.1 m height were connected using steel angle plates of size 200 mm × 100 mm × 6 mm and four numbers of 10 mm diameter bolts. The specimens were subjected to lateral loading to obtain the hysteresis curve, peak load–deflection, pseudo-ductile behavior, and energy dissipation. Base plates were used to avoid punching shear. Two specimens in each series of GFRP beam-column sections infilled with ECC-60P, ECC-70P, and ECC-80P were cast and tested at the end of 28 days. The results of GFRP beam-column sections infilled with HVFA-ECC were compared with those of pultruded GFRP beam-columns without infill. The details of the beam-column specimens are given in Table 7. The preparation of beam-column specimens is shown in Figure 5.

Table 7. Details of the GFRP beam-column specimens.

Sl. No.	Beam-Column ID	No of Specimens	Outer Material	Infill Material
1	BCG-H	2	GFRP Section	-
2	BCG-E60P	2	GFRP Section	ECC-60P
3	BCG-E70P	2	GFRP Section	ECC-70P
4	BCG-E80P	2	GFRP Section	ECC-80P

Figure 5. The casting of GFRP beam-column specimens.

2.4. Experimental Investigation

Lateral Loading on Pultruded GFRP Beam-Column with and without HVFA-ECC

GFRP beam-columns with and without HVFA-ECC infill consist of a 1.5 m long beam and a 1.1 m high column connected using steel angle plates and bolts. A schematic diagram of the experimental setup for beam-columns is shown in Figure 6.

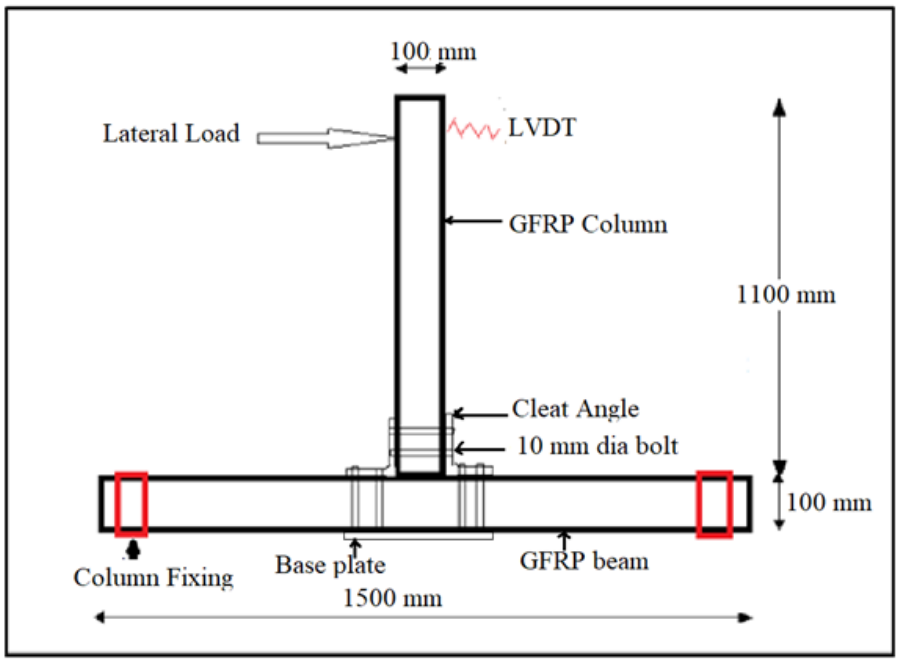

Figure 6. A schematic diagram of the experimental setup for beam-column testing.

The test was conducted on a reaction frame of 200 kN capacity having a stroke length of 100 mm. A hydraulic jack attached to the load cell was used for the measurement of the applied load on the column, and an LVDT was used for the measurement of lateral displacement at the top of the column, as shown in Figure 7. The lateral load and the corresponding displacement readings were obtained from the data logger connected to a computer, which captured the values until the completion of the test. Cyclic loading was applied on the top of the column until the specimen failed.

Figure 7. Experimental setup for lateral loading on beam-columns.

The test was conducted on a reaction frame of 200 kN capacity having a stroke length of ±100 mm. A hydraulic jack attached to the load cell was used for the measurement of the applied load on the column, and an LVDT was used for the measurement of lateral displacement at the top of the column, as shown in Figure 7. The lateral load and the corresponding displacement readings were obtained from the data logger connected to a computer, which captured the values until the completion of the test. Cyclic loading was applied on the top of the column until the specimen failed.

3. Results and Discussion

3.1. Lateral Load–Deformation Behavior

The failure of the GFRP beam-column without HVFA-ECC infill was sudden, but the failure of GFRP sections infilled with HVFA-ECC was in a sequential manner and exhibited a larger load-carrying capacity due to the confinement effect provided by ECC with the GFRP section. The failure pattern of the beam-column specimens is shown in Figure 8.

Figure 8. Failure pattern of beam-columns manufactured from GFRP infilled with and without HVFA-ECC.

Figure 9 shows the hysteretic curve of BCG-H specimens. The average ultimate load and maximum deflection of BCG-H specimens were 13.6 kN and 29.6 mm, respectively. When subjected to forward lateral loading, the BCG-E60P specimens recorded an average ultimate lateral load of 19.15 kN with a maximum lateral deflection of 51.2 mm. Figure 10 shows the hysteretic curve of BCG-E60P specimens. The BCG-E70P exhibited an ultimate load of 17.82 kN with a maximum lateral deflection of 45.80 mm. Figure 11 shows the

hysteretic curve of BCG-E70P specimens. The BCG-E80P failed with an average lateral load capacity of 16.35 kN with an average displacement of 38.35 mm. Figure 12 shows the hysteretic curve of BCG-E80P specimens.

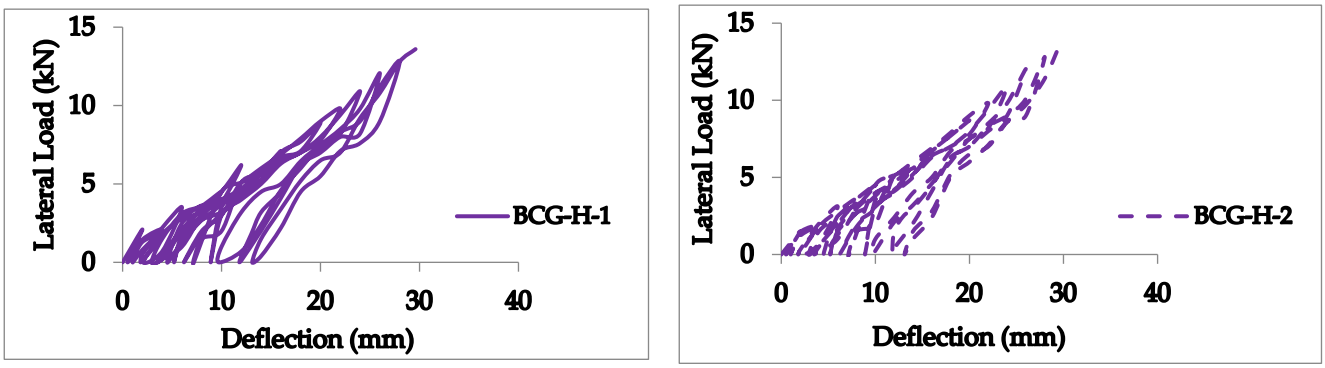

Figure 9. Hysteretic curves of hollow GFRP beam-columns. (**a**) Specimen 1; (**b**) specimen 2.

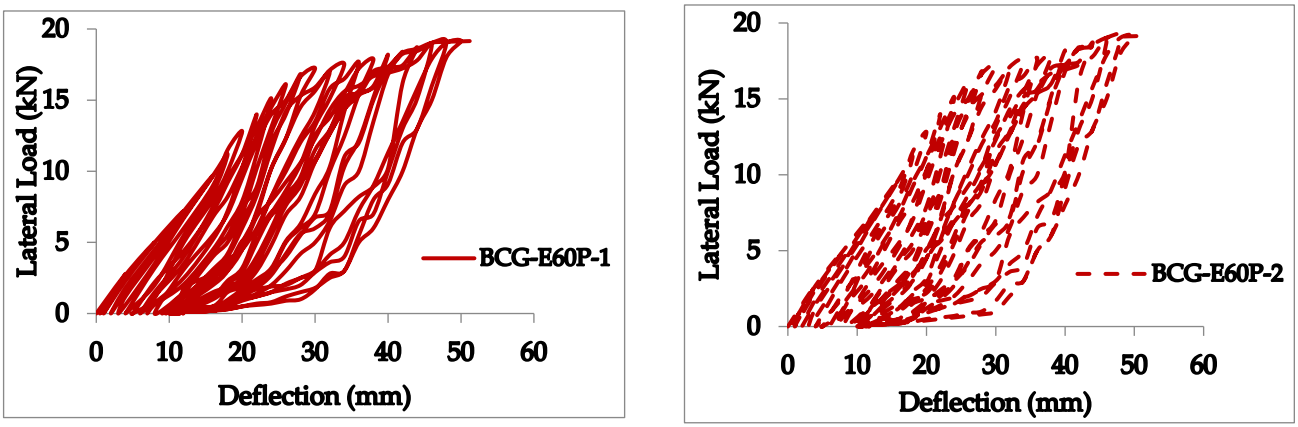

Figure 10. The hysteretic curve of the GFRP-ECC60P beam-column. (**a**) Specimen 1; (**b**) specimen 2.

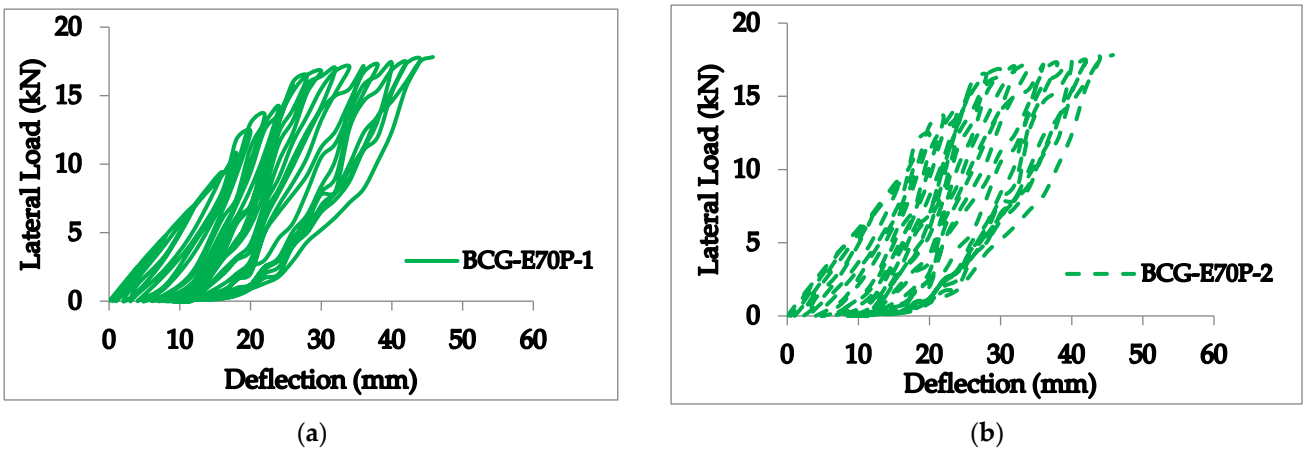

Figure 11. The hysteretic curve of the GFRP-ECC70P beam-column. (**a**) Specimen 1; (**b**) specimen 2.

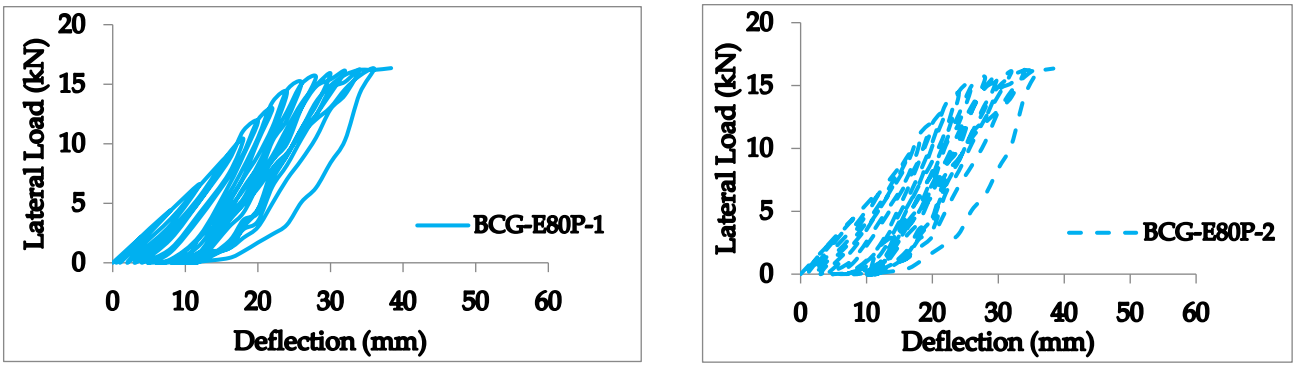

Figure 12. The hysteretic curve of the GFRP-ECC80P beam-column. (**a**) Specimen 1; (**b**) specimen 2.

3.2. Strength of the Beam-Column Specimens

Figure 13 depicts the cyclic envelope or P–Δ curves for the GFRP beam-column with or without HVFA-ECC. The lateral load capacity of the specimens is taken as the average of the load values when they were subjected to lateral loading in the forward direction. The BCG-H specimens attained an average ultimate lateral load of 13.6 kN with an average lateral displacement of 30 mm. The BCG-E60P specimens recorded an average lateral peak load of 19.5 kN with an average lateral displacement of 51.2 mm. The BCG-E70P specimens exhibited an average ultimate lateral strength of 17.82 kN with an average lateral displacement of 45.8 mm. The average lateral ultimate load of the BCG-E80P specimens was 16.35 kN with an average lateral displacement of 38.35 mm.

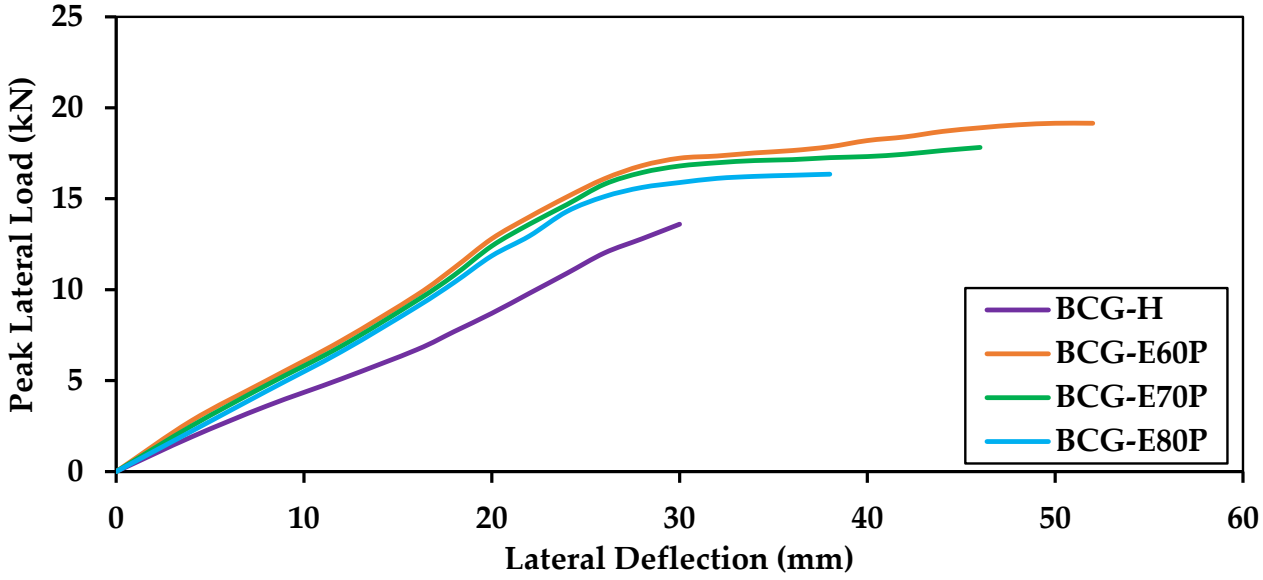

Figure 13. Cyclic envelope curve of GFRP with and without HVFA-ECC beam-columns.

3.3. Energy Dissipation Capacity

The dissipated energy in each cycle was calculated as the area bound by the hysteresis loop of that cycle from the load (P) versus displacement (Δ) curve, and the total dissipated energy is calculated as the summation of the energy dissipated in all the cycles up to the failure of the specimen. The energy dissipation curve of the beam-column is shown in Figure 14.

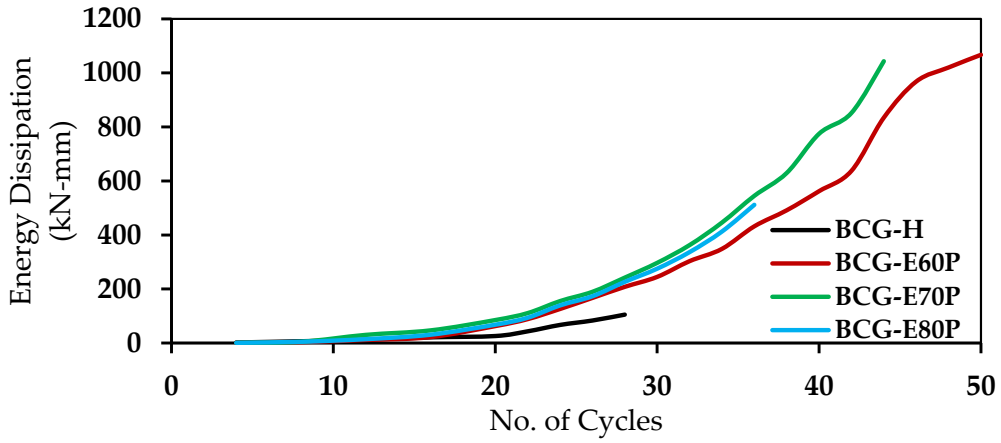

Figure 14. Energy dissipation curves.

The energy dissipation of BCG-H is 105 kN.mm. However, the energy dissipation of the BCG-E60P, BCG-E70P, and BCG-E80P was 1067 KN.mm, 1043 kN.mm, and 511 kN.mm, respectively. The energy dissipation of BCG-E60P observed was 10 times higher than that of the GFRP beam-column without infill.

3.4. "Pseudo-Ductile" Behavior

Ductility is one of the characteristics of a material that undergoes plastic deformations. However, non-plastic or non-ductile materials do not exhibit plasticity, and they could be characterized by a pseudo-ductility displacement index. The pseudo-ductility displacement index was calculated using the following Equation (1):

$$\mu = (d_u - d_y)/d_u \quad (1)$$

where μ—pseudo-ductility displacement index, d_u—failure displacement, d_y—displacement at yield.

However, the yield displacement is replaced by the displacement corresponding to the first peak load, while the failure displacement is assumed to be equal to the displacement corresponding to the last peak load of the load–displacement curve (just before the GFRP rupture). It should be pointed out that pseudo-ductility is not a measure of material plastic behavior, but rather an indicator of the post-peak load residual strength and concomitant deformation after significant damage in the material, component, or connection [37]. The values of μ of the beam-column tested are given in Table 8. BCG-E60P, BCG-E70P, and BCG-E80P respectively exhibited 67%, 48%, and 31% more pseudo-ductility than BCG-H.

Table 8. Pseudo-ductility index for all beam-column specimens.

Sl. No.	Beam-Column ID	d_u (mm)	dy (mm)	μ (-)
1	BCG-H	30	30	0
2	BCG-E60P	52	28	0.46
3	BCG-E70P	46	28	0.39
4	BCG-E80P	38	24	0.36

4. Numerical Investigations

Numerical investigations were carried out using Autodesk robot structural analysis (RSA) software. RSA is a structural analysis software that verifies different code compliance and uses build information modeling (BIM) integrated workflows to exchange data with other software. The RSA has wind simulation, extensive analysis capabilities, finite element analysis (FEA) with auto meshing, country-specific design standards, and an open and flexible application programming interface. The integration option in RSA enables the import of structural members and connection profiles from software such as Auto-CADD,

Revit, and Advanced Steel. The connection profiles from other software can also be imported to RSA.

4.1. Modeling and Meshing

The material properties of GFRP and HVFA-ECC imported into RSA were based on the results obtained from the test. Figure 15 shows the material properties assigned in the RSA software.

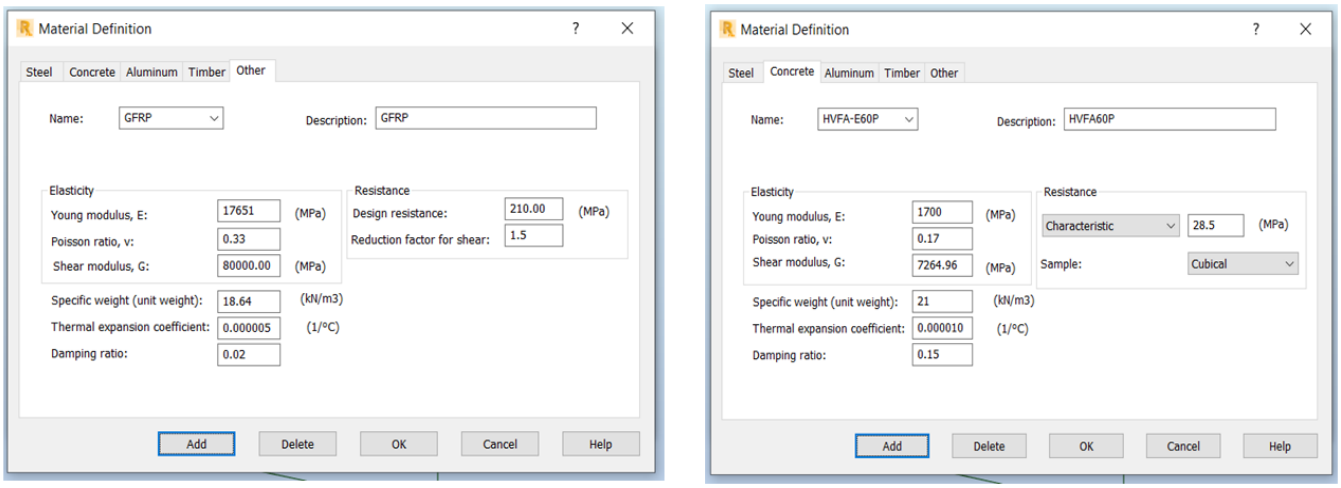

(**a**) (**b**)

Figure 15. Material properties used in the FE model. (**a**) GFRP; (**b**) HVFA-ECC.

The Section definition tool option in RSA enables the creation of composite sections with different materials. The GFRP sections infilled with HVFA-ECC were created and the material properties were assigned. The contact behavior between the GFRP and HVFA-ECC was modeled as Coulomb friction. The beam model of the GFRP sections was created using RSA software. Figure 16 shows the creation of the GFRP composite section and modeling of the beam-column made of the GFRP section with and without infill with HVFA-ECC. However, the connection profile of the beam-column was modeled in Autodesk advanced steel software and imported to RSA. Figure 17 shows the modeling of the connection profile in Autodesk advanced steel software.

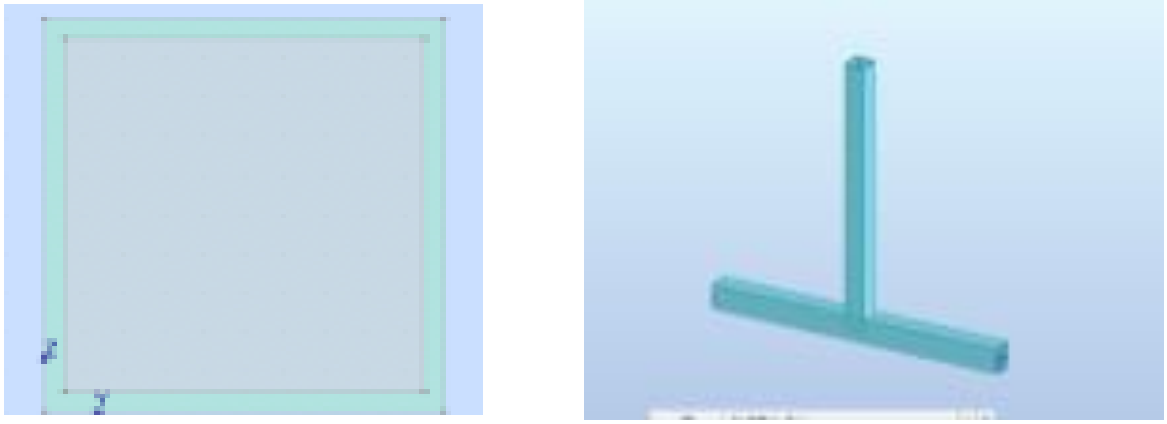

(**a**) (**b**)

Figure 16. Creation of GFRP sections. (**a**) Composite section; (**b**) modeling of beam-column in RSA.

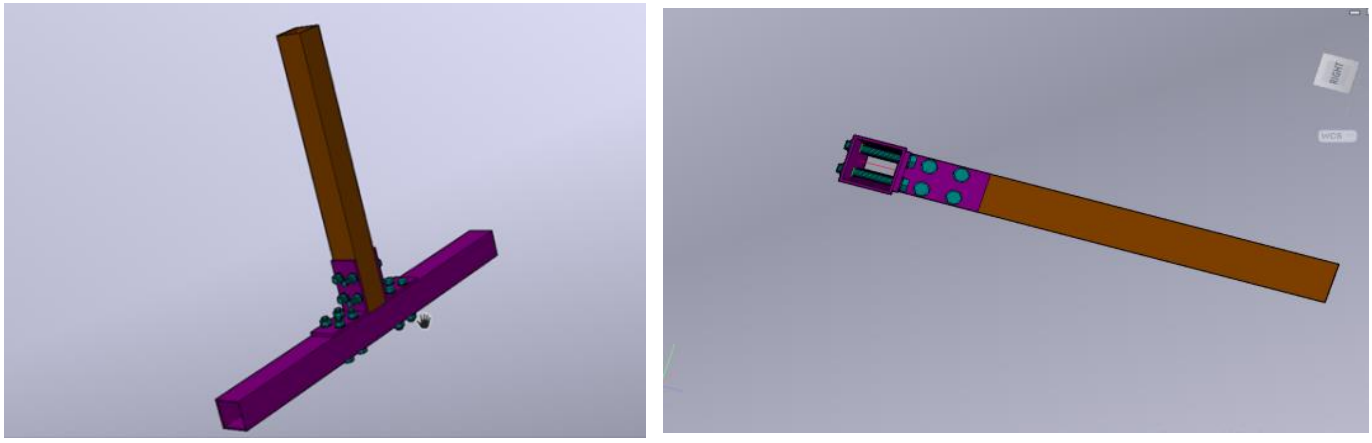

Figure 17. Creation of connection profile using Autodesk advanced steel software.

The coons meshing type with squares in rectangular contour meshing options were given to create meshing of the members. To obtain meshes with a fine size, four-noded quadrilaterals for surface and four-noded tetrahedrons for the volumetric type of meshing were given. Figure 18 shows the mesh type given and the meshing of the GFRP beam-column.

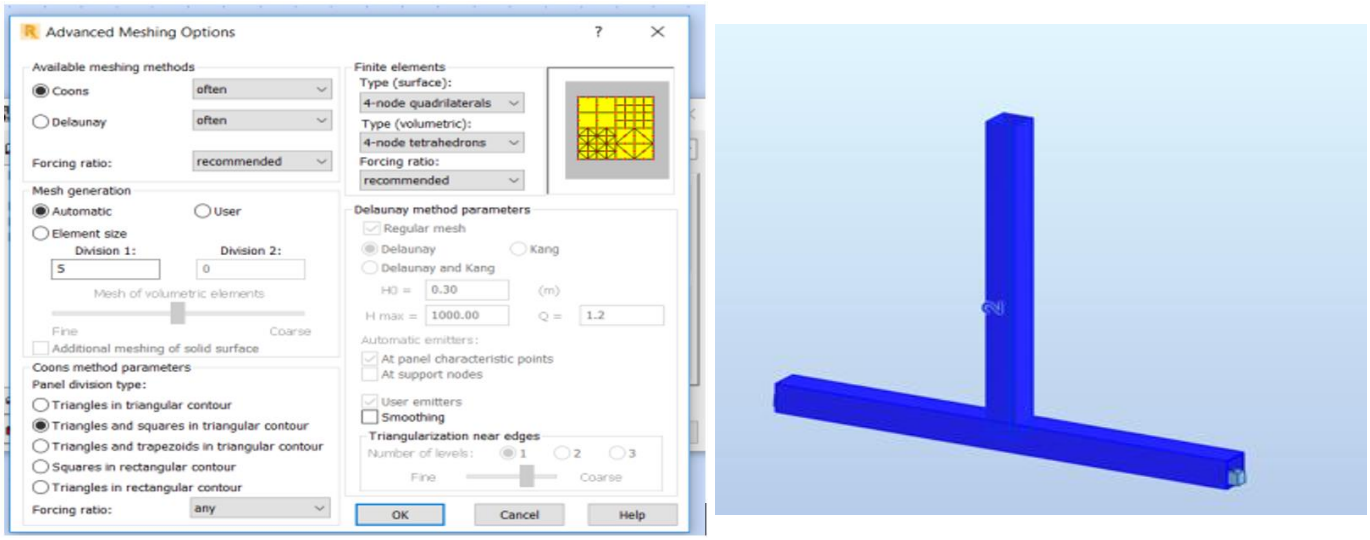

(**a**) (**b**)

Figure 18. Details of the FEA meshing. (**a**) Meshing data; (**b**) meshing of GFRP beam-column in RSA.

4.2. Support and Loading Condition

In the beam-column, both ends of the beam were assigned as fixed conditions, and the load was applied at the top of the column as applied in the experimental investigation. Nonlinear analysis was performed to understand the behavior of the GFRP beam-column. Figure 19 shows the support condition provided for the beam-column.

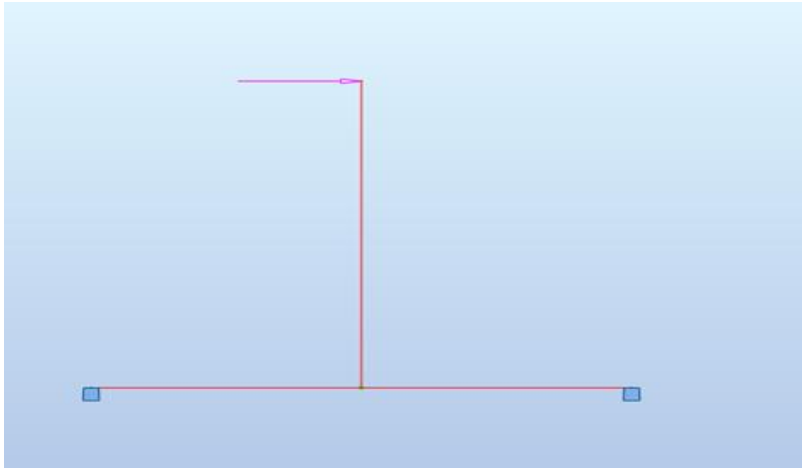

Figure 19. Support and loading condition of the beam-columns assigned in RSA.

4.3. Load–Deflection Behavior of Beam-Columns

The failure pattern of the BCG−H, BCG−E60P, BCG−E70P, and BCG−E80P beam-column is shown in Figure 20, obtained from RSA. The BCG−H exhibited an ultimate load of 12.98 kN, but BCG-E60P, BCG-E70P, and BCG-E80P showed a peak load of 17.70 kN, 19.09 kN, and 16.01 kN, respectively. Figure 21 shows the comparison of the load–deflection curves of the BCG-H, BCG-E60P, BCG-E70P, and BCG-E80P beam-columns obtained from experimental and analytical investigations.

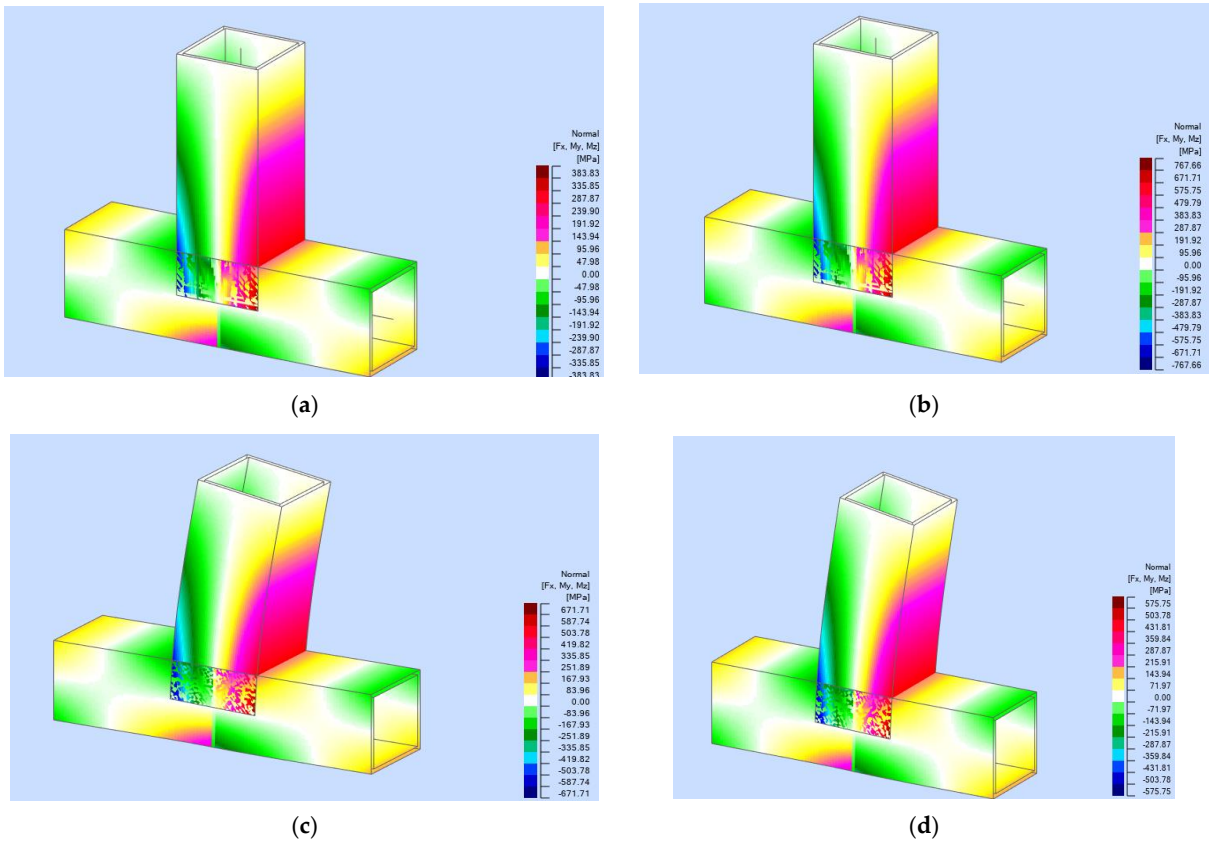

(**a**) (**b**)

(**c**) (**d**)

Figure 20. Failure modes of beam-columns obtained from the RSA. (**a**) BCG−H; (**b**) BCG−E60P; (**c**) BCG−E70P; (**d**) BCG−E80P.

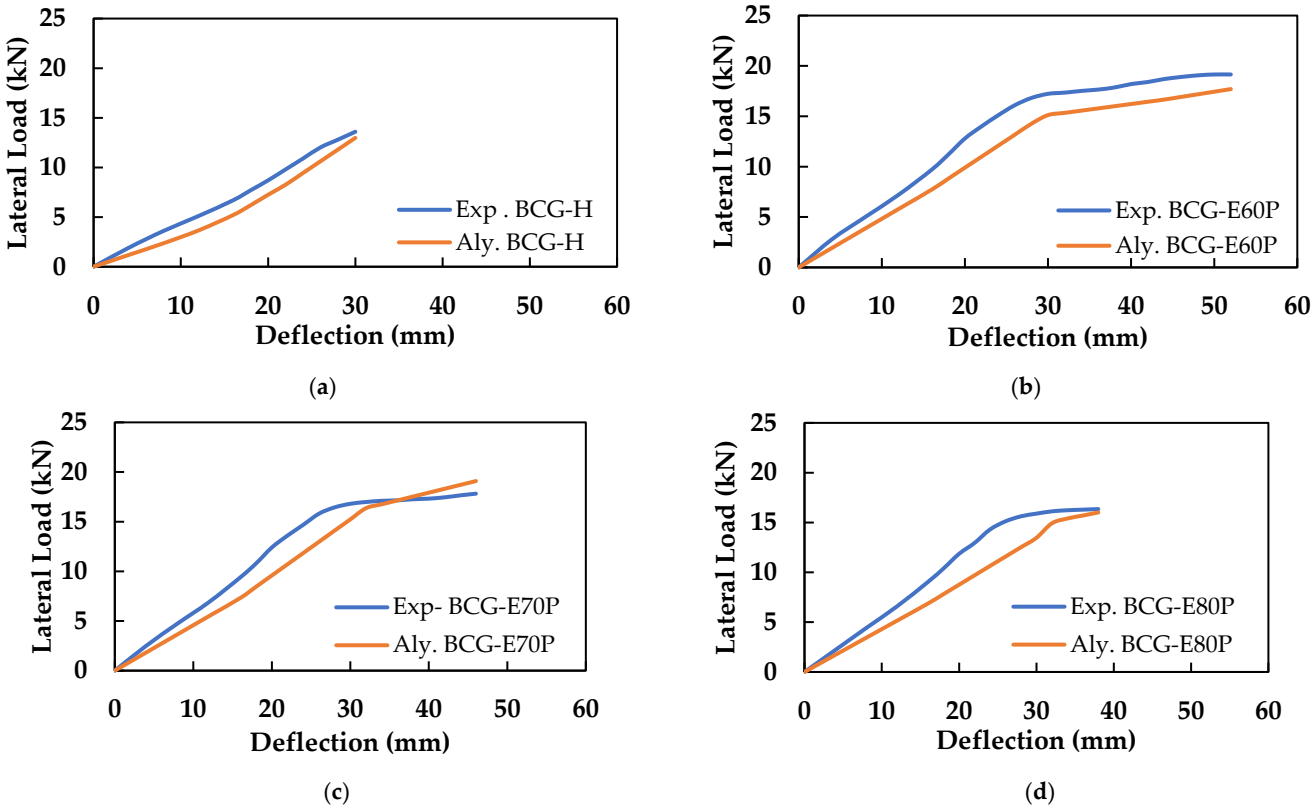

Figure 21. Comparison of load–displacement curves obtained from the experimental and numerical investigations. (**a**) BCG-H; (**b**) BCG-E60P; (**c**) BCG-E70P; (**d**) BCG-E80P.

5. Conclusions

Experimental and analytical investigations have been carried out on the performance of beam-columns made of a GFRP section with and without HVFA-ECC infill. Investigations into the mechanical properties of the GFRP section and HVFA-ECC were carried out. The GFRP beam-column load–displacement hysteretic behavior, capacity, pseudo-ductile behavior, and energy dissipation capacity are summarized below.

- The average ultimate tensile strength, compressive strength, elastic modulus, flexural strength, flexural modulus, shear strength, and shear modulus are 387.5 MPa, 150 MPa, 17.2 Mpa, 215 MPa, 1.1 GPa, 29 MPa, and 3 GPa, respectively.
- In the direct tensile strength test, the ultimate tensile strength of ECC-60P, ECC-70P, and ECC-80P was, respectively, 7%, 9%, and 11.5% less than ECC-0, and the ultimate tensile strains of ECC-60P, ECC-70P, and ECC-80P were 20% less than that of ECC-0.
- The average lateral load-carrying capacity of BCG-E60P, BCG-E70P, and BCG-E80P was found to be, respectively, 43%, 31%, and 20% higher than that of BCG-H.
- The energy dissipation of the BCG-E60P, BCG-E70P, and BCG-E80P beam-column specimens was, respectively, 100%, 39%, and 23% higher than that of the BCG-H specimen.
- Further, BCG-E60P, BCG-E70P, and BCG-E80P exhibited, respectively, 67%, 48%, and 31% more pseudo-ductility than BCG-H.
- ECC with fly ash up to 70% as a replacement for cement could be utilized in infilling the GFRP sections.
- The analytical results obtained from RSA show good agreement with the experimental results.

Thus, the GFRP beam-column infilled with high-volume ECC having cement replacement up to 70% with fly ash exhibited good lateral load-carrying capacity, energy dissipation capacity, and improved pseudo-ductility behavior compared with the hollow section. The use of high-volume fly ash, a byproduct of coal-burning power plants

used in the engineered cementitious composite used in ECC, reduces CO_2 emissions, and manufactured sand was used in ECC due to the scarcity of river sand.

Author Contributions: Y.C. and P.S.J.: Conceptualized the model, established the empirical theorem, and conducted the experiments. P.S.J., B.G.A.G., and K.R.: Supervised the research as well as the analysis of results. P.S.J., and K.K.: Introduced the idea of cyclic loading in this project, designed the beam-column, wrote, reviewed, and submitted the paper, and collaborated in and coordinated the research. P.S.J., B.G.A.G., and K.R.: Suggested and chose the journal for submission. P.S.J., B.G.A.G., and K.R.: Participated in the manuscript revision phase. All authors have read and agreed to the published version of the manuscript.

Funding: This research received no external funding.

Institutional Review Board Statement: Not applicable.

Informed Consent Statement: Not applicable.

Data Availability Statement: The data presented in this study are available on request from the corresponding author.

Conflicts of Interest: This manuscript has not been submitted to, nor is it under review by, another journal or other publishing venue. The authors have no affiliation with any organization with a direct or indirect financial interest in the subject matter discussed in the manuscript. The authors declare no conflict of interest.

References

1. Hollaway, L.C. A Review of the Present and Future Utilisation of FRP Composites in the Civil Infrastructure with Reference to Their Important In-Service Properties. *Constr. Build. Mater.* **2010**, *24*, 2419–2445. [CrossRef]
2. Singh, S.B.; Chawla, H. An Investigation of Material Characterization of Pultruded FRP H- and I-Beams. *Mech. Adv. Mater. Struct.* **2016**, *25*, 124–142. [CrossRef]
3. Landesmann, A.; Seruti, C.A.; Batista, E.D.M. Mechanical Properties of Glass Fiber Reinforced Polymers Members for Structural Applications. *Mater. Res.* **2015**, *18*, 1372–1383. [CrossRef]
4. da S. Santos Neto, A.B.; Lebre La Rovere, H. Flexural Stiffness Characterization of Fiber Reinforced Plastic (FRP) Pultruded Beams. *Compos. Struct.* **2007**, *81*, 274–282. [CrossRef]
5. Zaghloul, M.M.Y.M. Mechanical Properties of Linear Low-Density Polyethylene Fire-Retarded with Melamine Polyphosphate. *J. Appl. Polym. Sci.* **2018**, *135*, 46770. [CrossRef]
6. Zaghloul, M.M.Y.; Zaghloul, M.Y.M.; Zaghloul, M.M.Y. Experimental and Modeling Analysis of Mechanical-Electrical Behaviors of Polypropylene Composites Filled with Graphite and MWCNT Fillers. *Polym. Test.* **2017**, *63*, 467–474. [CrossRef]
7. Correia, J.R.; Branco, F.A.; Silva, N.M.F.; Camotim, D.; Silvestre, N. First-Order, Buckling and Post-Buckling Behaviour of GFRP Pultruded Beams. Part 1: Experimental Study. *Comput. Struct.* **2011**, *89*, 2052–2064. [CrossRef]
8. Vieira, P.R.; Carvalho, E.M.L.; Vieira, J.D.; Toledo Filho, R.D. Experimental Fatigue Behavior of Pultruded Glass Fibre Reinforced Polymer Composite Materials. *Compos. Part B Eng.* **2018**, *146*, 69–75. [CrossRef]
9. Zhang, S.; Caprani, C.C.; Heidarpour, A. Strain Rate Studies of Pultruded Glass Fibre Reinforced Polymer Material Properties: A Literature Review. *Constr. Build. Mater.* **2018**, *171*, 984–1004. [CrossRef]
10. Al-saadi, A.U.; Aravinthan, T.; Lokuge, W. Effects of Fibre Orientation and Layup on the Mechanical Properties of the Pultruded Glass Fibre Reinforced Polymer Tubes. *Eng. Struct.* **2019**, *198*, 109448. [CrossRef]
11. Sirajudeen, R.S.; Sekar, R. Buckling Analysis of Pultruded Glass Fiber Reinforced Polymer (GFRP) Angle Sections. *Polymers* **2020**, *12*, 2532. [CrossRef] [PubMed]
12. Fam, A.; Cole, B.; Mandal, S. Composite Tubes as an Alternative to Steel Spirals for Concrete Members in Bending and Shear. *Constr. Build. Mater.* **2007**, *21*, 347–355. [CrossRef]
13. Rozylo, P. Stability and Failure of Compressed Thin-Walled Composite Columns Using Experimental Tests and Advanced Numerical Damage Models. *Int. J. Numer. Methods Eng.* **2021**, *122*, 5076–5099. [CrossRef]
14. Liu, X.; Karami, B.; Shahsavari, D.; Civalek, Ö. Elastic Wave Characteristics in Damped Laminated Composite Nano-Scaled Shells with Different Panel Shapes. *Compos. Struct.* **2021**, *267*, 113924. [CrossRef]
15. Mohamed, H.M.; Masmoudi, R. Flexural Strength and Behavior of Steel and FRP-Reinforced Concrete-Filled FRP Tube Beams. *Eng. Struct.* **2010**, *32*, 3789–3800. [CrossRef]
16. Aydın, F.; Sarıbıyık, M. Investigation of Flexural Behaviors of Hybrid Beams Formed with GFRP Box Section and Concrete. *Constr. Build. Mater.* **2013**, *41*, 563–569. [CrossRef]
17. Muttashar, M.; Manalo, A.; Karunasena, W.; Lokuge, W. Influence of Infill Concrete Strength on the Flexural Behaviour of Pultruded GFRP Square Beams. *Compos. Struct.* **2016**, *145*, 58–67. [CrossRef]
18. Li, V.C. On Engineered Cementitious Composites (ECC). *J. Adv. Concr. Technol.* **2003**, *1*, 215–230. [CrossRef]

19. Yang, E.-H.; Li, V.C. Strain-Hardening Fiber Cement Optimization and Component Tailoring by Means of a Micromechanical Model. *Constr. Build. Mater.* **2010**, *24*, 130–139. [CrossRef]
20. Kang, S.-B.; Tan, K.H.; Zhou, X.-H.; Yang, B. Experimental Investigation on Shear Strength of Engineered Cementitious Composites. *Eng. Struct.* **2017**, *143*, 141–151. [CrossRef]
21. Sivanantham, P.; Gurupatham, B.G.A.; Roy, K.; Rajendiran, K.; Pugazhlendi, D. Plastic Hinge Length Mechanism of Steel-Fiber-Reinforced Concrete Slab under Repeated Loading. *J. Compos. Sci.* **2022**, *6*, 164. [CrossRef]
22. Şahmaran, M.; Bilici, Z.; Ozbay, E.; Erdem, T.K.; Yucel, H.E.; Lachemi, M. Improving the Workability and Rheological Properties of Engineered Cementitious Composites Using Factorial Experimental Design. *Compos. Part B Eng.* **2013**, *45*, 356–368. [CrossRef]
23. Pan, Z.; Wu, C.; Liu, J.; Wang, W.; Liu, J. Study on Mechanical Properties of Cost-Effective Polyvinyl Alcohol Engineered Cementitious Composites (PVA-ECC). *Constr. Build. Mater.* **2015**, *78*, 397–404. [CrossRef]
24. Meng, D.; Lee, C.K.; Zhang, Y.X. Flexural and Shear Behaviours of Plain and Reinforced Polyvinyl Alcohol-Engineered Cementitious Composite Beams. *Eng. Struct.* **2017**, *151*, 261–272. [CrossRef]
25. Lin, C.; Kayali, O.; Morozov, E.V.; Sharp, D.J. Development of Self-Compacting Strain-Hardening Cementitious Composites by Varying Fly Ash Content. *Constr. Build. Mater.* **2017**, *149*, 103–110. [CrossRef]
26. Jia, Y.; Zhao, R.; Liao, P.; Li, F.; Yuan, Y.; Zhou, S. Experimental Study on Mix Proportion of Fiber Reinforced Cementitious Composites. *AIP Conf. Proc.* **2017**, *1890*, 020002. [CrossRef]
27. Rajamony Laila, L.; Gurupatham, B.G.A.; Roy, K.; Lim, J.B.P. Effect of Super Absorbent Polymer on Microstructural and Mechanical Properties of Concrete Blends Using Granite Pulver. *Struct. Concr.* **2020**, *22*, E898–E915. [CrossRef]
28. Yu, J.; Mishra, D.K.; Wu, C.; Leung, C.K. Very High Volume Fly Ash Green Concrete for Applications in India. *Waste Manag. Res. J. A Sustain. Circ. Econ.* **2018**, *36*, 520–526. [CrossRef]
29. Shanour, A.S.; Said, M.; Arafa, A.I.; Maher, A. Flexural Performance of Concrete Beams Containing Engineered Cementitious Composites. *Constr. Build. Mater.* **2018**, *180*, 23–34. [CrossRef]
30. Ismail, M.K.; Abdelaleem, B.H.; Hassan, A.A.A. Effect of Fiber Type on the Behavior of Cementitious Composite Beam-Column Joints under Reversed Cyclic Loading. *Constr. Build. Mater.* **2018**, *186*, 969–977. [CrossRef]
31. Pakravan, H.R.; Ozbakkaloglu, T. Synthetic Fibers for Cementitious Composites: A Critical and In-Depth Review of Recent Advances. *Constr. Build. Mater.* **2019**, *207*, 491–518. [CrossRef]
32. Wang, Q.; Lai, M.H.; Zhang, J.; Wang, Z.; Ho, J.C.M. Greener Engineered Cementitious Composite (ECC)—The Use of Pozzolanic Fillers and Unoiled PVA Fibers. *Constr. Build. Mater.* **2020**, *247*, 118211. [CrossRef]
33. Li, S.W.V.C.; Wu, C. Tensile Strain-Hardening Behavior of Polyvinyl Alcohol Engineered Cementitious Composite (PVA-ECC). *ACI Mater. J.* **2001**, *98*, 483–492. [CrossRef]
34. Rajamony Laila, L.; Gurupatham, B.G.A.; Roy, K.; Lim, J.B.P. Influence of Super Absorbent Polymer on Mechanical, Rheological, Durability, and Microstructural Properties of Self-Compacting Concrete Using Non-Biodegradable Granite Pulver. *Struct. Concr.* **2020**, *22*, E1093–E1116. [CrossRef]
35. Yoganantham, C.; Joanna, P.S. Effect of High Volume Fly Ash Concrete in Self-Curing Engineered Cementitious Composite (ECC). *Int. J. Adv. Res. Sci. Eng. Technol.* **2020**, *11*, 268–276. [CrossRef]
36. Lowe, D.; Roy, K.; Das, R.; Clifton, C.G.; Lim, J.B.P. Full Scale Experiments on Splitting Behaviour of Concrete Slabs in Steel Concrete Composite Beams with Shear Stud Connection. *Structures* **2020**, *23*, 126–138. [CrossRef]
37. Yang, E.-H.; Yang, Y.; Li, V.C. Use of High Volumes of Fly Ash to Improve ECC Mechanical Properties and Material Greenness. *ACI Mater. J.* **2007**, *104*, 620–628. [CrossRef]
38. Tosun-Felekoğlu, K.; Gödek, E.; Keskinateş, M.; Felekoğlu, B. Utilization and Selection of Proper Fly Ash in Cost Effective Green HTPP-ECC Design. *J. Clean. Prod.* **2017**, *149*, 557–568. [CrossRef]
39. Yoganantham, C.; Helen Santhi, M. Performance of Self-Compacting Self Curing Concrete with Fly Ash and M Sand. *Int. J. Earth Sci. Eng.* **2015**, *8*, 491–497.
40. Thiruchelve, S.R.; Sivakumar, S.; Raj, M.; Shanmugaraja, G.; Nallathambi, M. Effect of Polyethylene Glycol as Internal Curing Agent in Concrete. *Int. J. Innov. Res. Sci. Eng. Technol.* **2017**, *6*, 3521–3524.
41. Ascione, F.; Lamberti, M.; Razaqpur, A.G.; Spadea, S.; Malagic, M. Pseudo-Ductile Failure of Adhesively Joined GFRP Beam-Column Connections: An Experimental and Numerical Investigation. *Compos. Struct.* **2018**, *200*, 864–873. [CrossRef]
42. Madan, C.S.; Munuswamy, S.; Joanna, P.S.; Gurupatham, B.G.A.; Roy, K. Comparison of the Flexural Behavior of High-Volume Fly AshBased Concrete Slab Reinforced with GFRP Bars and Steel Bars. *J. Compos. Sci.* **2022**, *6*, 157. [CrossRef]
43. Madan, C.S.; Panchapakesan, K.; Anil Reddy, P.V.; Joanna, P.S.; Rooby, J.; Gurupatham, B.G.A.; Roy, K. Influence on the Flexural Behaviour of High-Volume Fly-Ash-Based Concrete Slab Reinforced with Sustainable Glass-Fibre-Reinforced Polymer Sheets. *J. Compos. Sci.* **2022**, *6*, 169. [CrossRef]
44. Yoganantham, C.; Joanna, P.S. Flexural Behaviour of Pultruded GFRP Beams Infilled with HVFA ECC. *Mater. Today Proc.* **2021**, *45*, 5978–5981. [CrossRef]
45. *ASTM D3039*; International Standard Test Method for Tensile Properties of Polymer Matrix Composite Materials. ASTM International: West Conshohocken, PA, USA, 2007.
46. *ASTM D3410*; Standard Test Method for Compressive Properties of Polymer Matrix Composite Materials with Unsupported Gage Section by Shear Loading. ASTM International: West Conshohocken, PA, USA, 2016.

47. *ASTM D790*; Standard Test Methods for Flexural Properties of Unreinforced and Reinforced Plastics and Electrical Insulating Materials. Astm International: West Conshohocken, PA, USA, 2010.
48. *ASTM D2344*; Standard Test Method for Short-Beam Strength of Polymer Matrix Composite Materials and Their Laminates. ASTM International: West Conshohocken, PA, USA, 2013.
49. *ASTM C1273*; Standard Test Method for Tensile Strength of Monolithic Advanced Ceramics at Ambient Temperatures. ASTM International: West Conshohocken, PA, USA, 2015.